CONFERENCE PRE-PRINT

OVERVIEW OF ST40 RESULTS AND FUTURE: EXPANDING THE PHYSICS BASIS OF HIGH-FIELD SPHERICAL TOKAMAKS

O. ASUNTA ON BEHALF OF ¹THE ST40 TEAM Tokamak Energy Ltd.
Milton Park, Oxfordshire, United Kingdom of Great Britain and Northern Ireland Email: otto.asunta@tokamakenergy.com

Abstract

The goal of the ST40 programme is to explore the physics of high-field spherical tokamaks (STs), to validate empirical and theoretical models and, hence, to build confidence in predictions required to support the design of future generations of STs. ST40 is a compact ST with the following parameters: $R_0 \approx 0.4$ –0.5m, $I_p \approx 0.25$ –0.8MA, $B_t(R=0.4\text{m}) \approx 0.7$ –2.1T, $\kappa < 2.0$, and $A \approx 1.6$ –1.9. Highlights of recent experimental results include (i) H-mode and confinement studies at $B_t \leq 2.1\text{T}$, (ii) observation of bifurcation of the scrape-off-layer power fall-off width, λ_q , into a 'wide' branch that follows existing H-mode scalings and a 'narrow' branch that exhibits λ_q values that are up to 10 times lower that the predictions of established scalings, (iii) development of high-performance scenarios with plasma current, I_p , up to 800kA, and (iv) first ST40 experiments utilising the newly commissioned impurity powder dropper. The work on all these topics has been supported by a number of advancements in ST40 hardware and software, from plasma control to data analysis and interpretation. Next, before the end of 2025, ST40 will embark on a major upgrade to further expand its capabilities by introducing 1MW of radiofrequency heating, a pellet injector, and a pair of lithium evaporators for wall conditioning, among other improvements.

1. INTRODUCTION

The goal of the ST40 programme is to explore the physics of high-field spherical tokamaks (STs), to validate, empirical and theoretical models and, hence, to build confidence in predictions required to support the design of future generations of STs. The main research areas of the ST40 programme include: (i) transport and confinement, (ii) power exhaust, (iii) solenoid-free plasma start-up schemes, and (iv) high-performance scenarios. Beyond scientific research, another important aspect of the ST40 programme is supporting technology development.

ST40 is designed, built, and operated by Tokamak Energy Ltd., a private company based in Oxfordshire, UK. Recently, the research on ST40 has focused on the following aspects of high-field ST physics: developing diverted H-mode scenarios, studying confinement in a high-field ST, and investigating the scrape-off-layer power fall-off width. There has also been an effort to develop highly non-inductive, high β_p , operating scenarios. Before the end of 2025, ST40 will embark on a major upgrade, funded primarily by a cross-governmental public-private partnership between Tokamak Energy, the U.S. Department of Energy, and UK Department of Energy Security and Net Zero [2]. The aim of the upcoming upgrade is to increase the relevance of ST40 results for the next generation of STs by (i) moving from graphite to metal plasma-facing components (PFCs), (ii) exploring the use of lithium, a potential future liquid metal plasma-facing material, in the form of evaporative solid lithium coatings on PFCs, (iii) further increasing the toroidal magnetic field of ST40, (iv) introducing radiofrequency (RF) heating and current drive, and (v) enabling core fuelling via a pellet injector. To take full advantage of plasma operations after these upgrades, the ST40 diagnostic suite will also be overhauled by both adding a host of new diagnostics and refining many of the existing ones.

This manuscript gives an overview of progress made on ST40 in the past two years. Its structure is as follows. Section 2 introduces ST40 and highlights some of its new features from hardware to real-time software and from post-pulse data analysis and interpretation to modelling capabilities. Sections 3 to 6 summarise experimental results from ST40 on transport and confinement, including extending ST confinement scaling to higher toroidal fields (Sec. 3), high-performance operating scenarios (Sec. 4), scrape-off-layer and divertor (Sec. 5), and lithium experiments using a newly commissioned impurity powder dropper (Sec. 6). Finally, Section 7 outlines the plans

-

¹ For a full list of authors, see [1].

for the upcoming upgrade. It also presents a summary of recent RF scenario modelling that underlines the benefits of increased toroidal field for electron cyclotron (EC) current drive and heating.

2. ST40

2.1. Overview

ST40 is a spherical tokamak with copper magnets. Its defining feature is the high toroidal magnetic field: ST40 often operates at B_t =2.1T at major radius of R_0 =0.4m, which is more than two times higher than any other ST. The main parameters achieved by ST40 are R0 \approx 0.4–0.5m, Ip \approx 0.25-0.8MA, Bt(R=0.4m) $\approx 0.7-2.1$ T $\kappa < 1.9$, and A $\approx 1.6-1.9$. A crosssection of ST40 is presented in Fig. 1. For plasma start-up, ST40 uses the merging-compression (MC) process [3][4], in which the two high voltage in-vessel MC coils are used to create two helical plasma rings that then merge and get 'compressed' radially inward to form a conventional spherical tokamak plasma. The major benefit of utilising the MC start-up, especially in a compact device like ST40, is that it can produce ~0.5MA of plasma current in about 6ms without using any of the ~200mVs of flux that the ST40 central solenoid can provide. Using the central solenoid, the plasma current can be ramped up further to up to 850kA or, alternatively, the plasma current flattop at $I_p = 450kA$ extended up to 200ms.

For auxiliary heating and current drive, ST40 has two co-current deuterium neutral beam injectors (NBIs) that deliver up to 1.0MW and 0.8MW of auxiliary heating power at beam energies of 55keV and 24keV. The maximum durations of the beams at full power are currently 1s and 90ms, respectively. Thanks to recent upgrades, at 80% of the power, the 24keV beam can be extended up to 140ms.

ST40 is equipped with a wide array of diagnostics including (i) active and passive spectroscopy for ion temperature and rotation measurements as well as impurity monitoring, (ii) Thomson scattering and

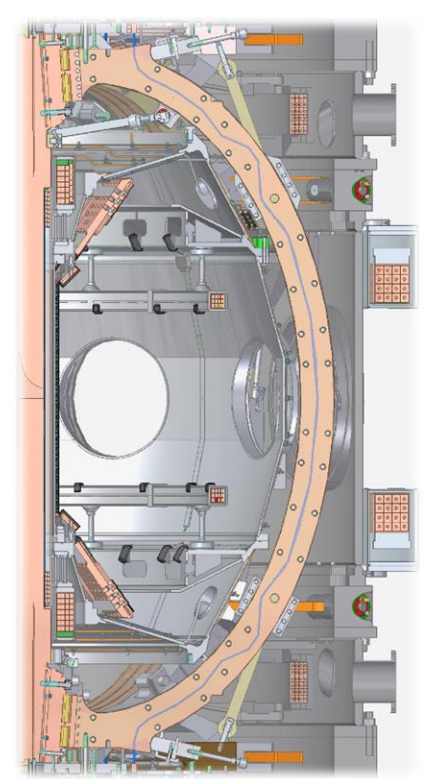


FIG. 1. Cross-section of ST40

interferometers for electron temperature and density measurements, (iii) neutral particle and neutron detectors, (iv) radiation diagnostics, (v) cameras, (vi) magnetic diagnostics, and so on. A complete list of the current diagnostics suite and data analysis can be found from [1], whereas the latest improvements are introduced in Sec. 2.2 and the upcoming upgrades and additions to the ST40 diagnostics suite are outlined in Sec. 7.7.

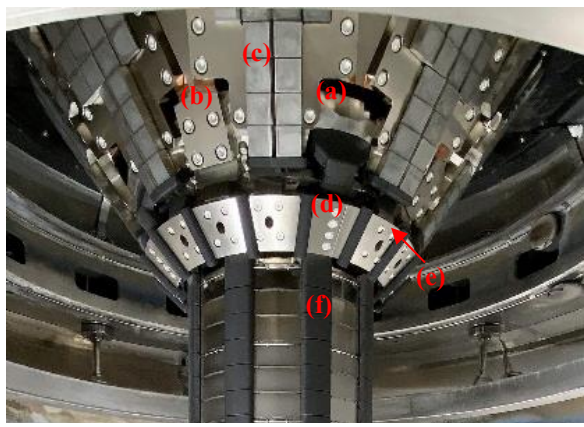


FIG. 2. A photo of the ST40 divertor and the centre column highlighting (a) a carrier, (b) a bridging plate, (c) a divertor tile, (d) a passive stabilisation ring, (e) a protective graphite cuff, and (f) a graphite limiter tile.

ST40 is designed to operate in a double-null diverted configuration and, therefore, has both an upper and a lower divertors. The divertor assemblies consist of eight (8) nickel-plated copper carriers and eight (8) nickelplated copper bridging plates that house the divertor tiles. All these elements are identified in Fig. 2. Each divertor tile consists of a 4mm molybdenum plate, as the plasmafacing material, brazed on a copper-chrome-zirkonium (CuCrZr) base. The elements of the divertor assembly, the carriers and the bridging plates, are electrically connected to each other and create a conducting path for induced currents in the toroidal direction. Therefore, the copper in the divertor assembly serves two purposes: it acts as a heat sink and provides passive stabilisation against plasma instabilities. The electrical conductivity of each divertor assembly was adjusted using gaskets between the carriers and the bridging plates. A pair of passive stabilisation rings, made of nickel-plated aluminum alloy 5083 and protected by graphite cuffs, is

located at the end of the centre column (see Fig. 2.). The eight (8) centre column limiters are made of graphite, as are the neutral beam dumps and sets of protective bumpers on the MC coils and the shelves supporting them, shown in black in Fig. 1.

2.2. New features

Many improvements have been made on ST40 hardware and, even more so, software over the past couple of years. One of the hardware additions was the installation and commissioning of an impurity powder dropper (IPD). IPD is used to deliver material in the form of a powder into the plasma, typically to study its effect on the plasma edge. In IPD, the powder is placed on a vibrating drum actuated by a piezoelectric motor. The amount of powder delivered into the plasma through a slit in the drum is controlled by controlling the amplitude of the vibrations. The ST40 IPD has two independent drums, and it has been used to drop boron and lithium powder.

ST40 real-time control capabilities have recently been enhanced by upgrading the power supply configuration of the in-vessel merging-compression (MC) coils. The MC coils in an ideal location from plasma vertical control point of view (see Fig. 1). Connecting a real-time controllable low-voltage (520V) power supply unit (PSU) to them in an anti-series configuration, through a pair of 1Ω resistors, has allowed using the MC coils for both plasma start-up (high-voltage PSU, coils in series) and vertical control (low-voltage PSU, coils in anti-series). By using a cascade controller in ST40 Plasma Control System (PCS), this hardware arrangement has been utilised to control both plasma vertical velocity, v_Z , and the plasma current centroid vertical position, Z_C .

To further improve the post-pulse analysis and plasma control capabilities of ST40, two in-house open-source equilibrium reconstruction codes have been developed: GSFit [5,6] for post-pulse analysis, and a real-time capable version, RT-GSFit [7] to be used during a pulse. GSFit combines the flexibility and ease of use of Python with performance and robustness of Rust, and it has been successfully benchmarked against EFIT [8]. It is used in post-pulse analysis in magnetics-only mode with passive conductors. Using kinetic constraints is possible, as is a flexible choice for the degrees of freedom for pressure and poloidal current source functions. RT-GSFit is designed to calculate the magnetic reconstruction with millisecond resolution to enable real-time shape control on ST40. It is written in C to allow seamless integration with ST40 PCS, implemented in MathWorks® MATLAB/Simulink [9][9]. RT-GSFit has been verified offline against GSFit, and against an analytic solution to the Grad-Shafranov equation. Integration of RT-GSFit into ST40 PCS is on-going.

The ST40 post pulse analysis chain (PPAC) software, responsible for inter-pulse data analysis and interpretation, has also been improved [10]. PPAC, now managed by SLURM workload manager [11], executes 70+ analysis scripts written in Python, MATLAB, Fortran and IDL. The modular architecture of PPAC simplifies the integration and testing of new diagnostics analysis tools, while SLURM efficiently deals with resource allocation and dependencies between analysis tools. Together they offer a scalable and adaptable model for delivering reliable and quick inter-pulse analysis.

Analysis and interpretation capabilities for existing diagnostics have been expanded. As new analyses have been developed, they have been, wherever possible, included in PPAC to speed up interpretation and learning during experiment execution. The divertor Langmuir probe analysis has been updated to utilise GSFit [5] or EFIT [8] to calculate the angles between the probe surfaces and intersecting magnetic lines. Addition of these angles in the analysis enables improved estimates of electron density and parallel heat flux in the ST40 divertor on the timescales of the probe sweep frequency (~4kHz).

Inversion of foil and AXUV diode bolometry provide the total core radiated power profiles (Fig. 3(a) and (c)) necessary for power-balance analysis. The AXUV diodes will soon be cross-calibrated against foil bolometry to provide profiles with higher spatial and temporal resolution. Joint inversion of all the bolometric measurements installed on ST40 (32 unfiltered AXUV diode channels and 20 foil bolometry channels) will further expand the capabilities and resilience[12],[13]. Automatic profile fitting of Thomson scattering (TS) profile data (Fig. 3(e) and (f)) is included in PPAC, together with a data quality assessment. Using the automatic TS fitting output, effective charge, Zeff, profiles are computed in PPAC from visible Bremsstrahlung measured by ST40's CXRS spectrometers [14].

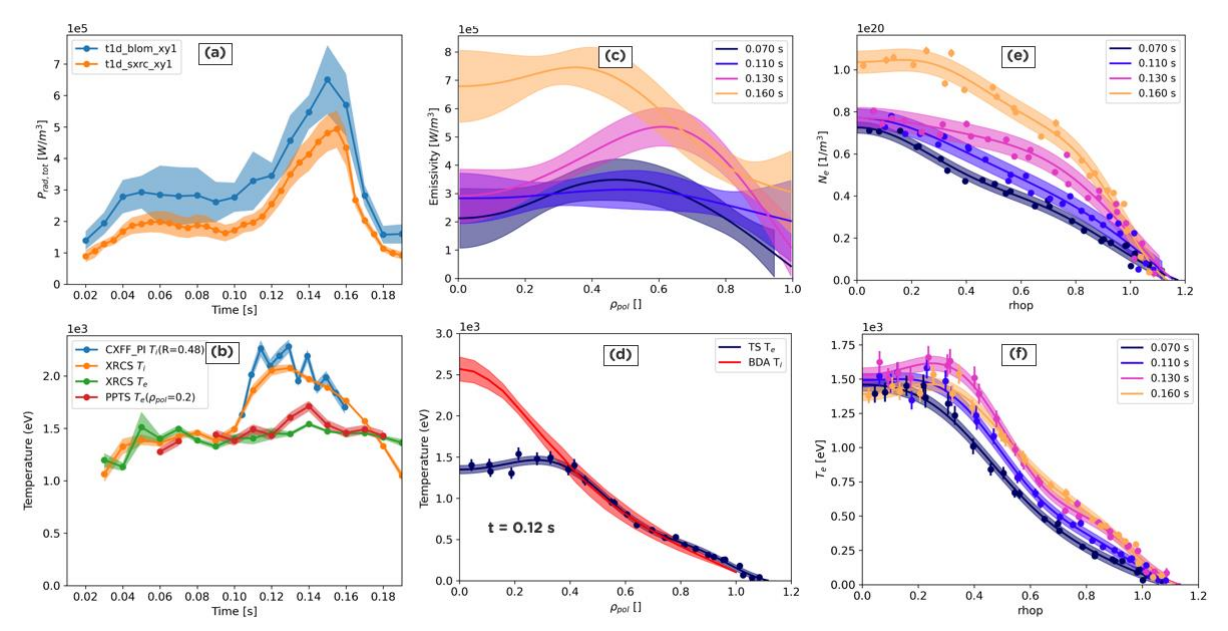


FIG. 3. Example core diagnostic measurements and interpretation for pulse #11419. Time evolution of total core radiated power from foil and AXUV bolometry (a), central ion and electron temperature measurements from CXRS, XRCS and TS (b). Total radiated power profile from foil bolometry (c). Ion temperature profile inference at 0.12 s using XRCS and CXRS measurements compared to TS electron temperature (d). Electron density (e) and temperature (f) profiles from TS.

Various charge exchange spectrometers (CXRS) measuring C, Ne, B, He, and D provide information on the central ion temperature. Given the complexity of these analyses, while an automatic version is included in PPAC, a detailed full-fit analysis is performed manually to guarantee the highest possible data quality. Additionally, due to the limited spatial coverage of the current CXRS systems [15],[16], Bayesian analysis workflows are employed to infer the ion temperature profiles Fig. 3(d)) by combining CXRS, X-ray Crystal spectrometer (XRCS) and TS measurements [17] [17],[14]. Bayesian inference workflows are being expanded to evaluate core radiation profiles as well as impurity plasma composition. Time evolution of several impurities is also analysed using data from an overview passive visible-UV spectrometer. This enables long-term tracking of the effects of plasma conditioning (e.g., boronisations and He glow discharge cleaning (GDC)) and spotting unexpected events such as leaks of fluorine influx due to damage to cable insulation. In all these analysis workflows, automatic and manual, workflow managers guarantee that upstream dependencies are captured in the database and that consistency is maintained.

Another integrated modelling tool that has been developed, partly in support of ST40 operations, is a tokamak simulator SOPHIA[18] [18]. It couples the ASTRA-SPIDER free boundary evolution and transport code [19-21], a plasma control system, and models of actuators and diagnostics. For ST40 applications, e.g. scenario design [18], ST40 PCS is used to control the ASTRA-SPIDER plasma model. SOPHIA is fully integrated with the ST40 tools for pulse scheduling, data storage and access, and plotting and analysis. Consequently, pulses prepared for SOPHIA can be run on ST40, and vice versa, and simulated and experimental data readily compared. This makes SOPHIA a great training tool for staff and students alike. SOPHIA can be adapted to any tokamak and has been used for scenario validation and controller design to support Tokamak Energy's future device design efforts.

3. TRANSPORT AND CONFINEMENT

3.3. LH transition and H-mode properties

High confinement mode (H-mode) operation has been routinely achieved in ST40 in both double-null-diverted (DND) and upper-single-null (USN) magnetic configurations utilising one or both of ST40 NBI systems. ST40 plasmas typically transition into H-mode shortly after entering diverted configuration, 30-80ms into the pulse, with line-averaged L-mode densities of $< n_e > \sim 3$ -6e19 m⁻³. By optimising the PF coil waveforms, even earlier entry into DND configuration, soon after the MC startup, has been achieved.

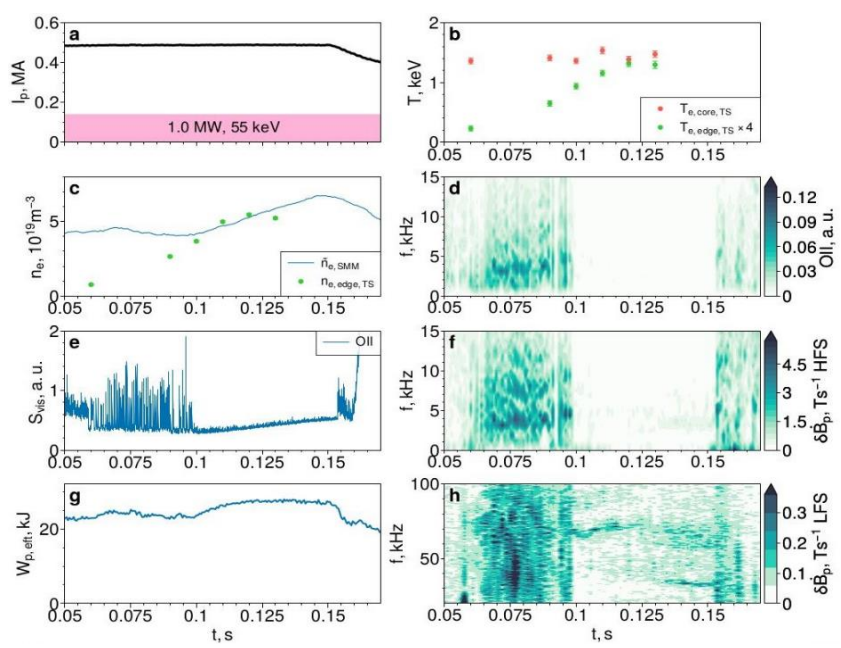


FIG. 4. Pulse #13706. (a) Plasma current and NBI power. (b) Core (0.621m) and edge (0.795m) electron temperatures measured by Thomson Scattering. (c) Line averaged electron density measured by the SMM interferometer and edge electron density measured by TS. Spectrograms of emission near OII line (441.5 nm) (d), midplane HFS (f) and LFS (h) magnetic probes. (e) Visible light from midplane OII emission (blue). (g) Plasma stored energy from EFIT. I-phase at 60-99ms, ELM-free H-mode at 100-155ms.

In many pulses, the L- to Hmode transition happens via an intermediate state that has been identified as I-phase [22-24]. The presence of I-phase indicates proximity to the L-H power threshold and characterised by oscillations in the kHz range in various plasma signals: electron density, visible emission, poloidal magnetic field. The I-phase state has also been observed without a transition to H-mode. example of a pulse with an L-H transition through an I-phase is depicted in Fig. 4. In this pulse, the I-phase period lasts from 60 to 99ms, with the transition to ELM-free H-mode at the end of it. The frequency of limit-cycle oscillations (LCOs) is around 3kHz in the beginning of I-phase and increases to 4.5kHz prior to the H-mode transition. Both edge electron density temperature increase throughout

the I-phase leading to the transition. The frequency of LCOs was found to increase with the edge electron temperatures.

Plasmas in ELM-free H-modes are usually characterised by the presence of a quasi-coherent mode at high frequencies in the range from several tens of kilohertz to above a hundred of kilohertz. The mode is strongest on the LFS midplane magnetic probe (Fig. 4(h)). During ELM-free H-mode the pedestal electron densities and temperatures increase sharply, with the profiles indicating an edge transport barrier (Fig. 5). The discharge #13706 is characterised by triangularity of $<\delta>=0.5$, elongation of $\kappa=1.7$. Plasma shaping is widely shown to be key in accessing type-I ELM-free regimes, such as QH-mode on DIII-D [25], EDA H-mode on Alcator C-mod [26], QCE on ASDEX-U, TCV and JET [27]. The observed mode of an electromagnetic nature could be responsible for enhanced transport in the pedestal limiting the pressure gradients reaching ideal peeling-ballooning limits.

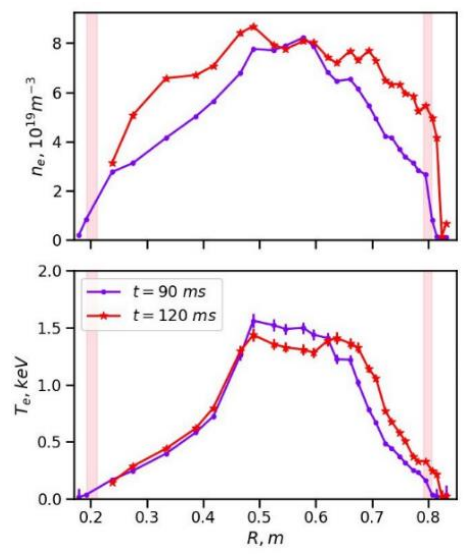


FIG. 5. Electron density (top) and temperature (bottom) profiles measured by Thomson scattering during I-phase (90ms) and ELM-free H-mode (120ms).

3.4. Confinement scalings

Quality of confinement is a strong determinant of the size of future fusion power plant and, therefore, its capital cost [28]. Earlier, thermal energy confinement, τ_E , in STs at $B_t < 1T$, has been found to be characteristically different from that observed in large aspect ratio tokamaks [29]: a linear scaling of energy confinement time with B_t has been demonstrated in NSTX, MAST and GLOBUS-M(2) H-mode [30-32].

On ST40, experiments with a B_t scan from 0.55T to 1.7T at the plasma geometric axis were carried out both in L- and H-mode plasmas. A diverted ST40 H-mode scenario with I_p = 390kA and 1MW of NBI heating was used as a starting point for the B_t scan. L-mode plasmas were obtained by puffing in Ar impurity at the marginal to L-H transition stage, and the additional radiated power kept the plasmas below the L-H transition threshold. Plasma density was kept roughly constant throughout the scan. The electron temperature T_c was, however, found to increase with B_t . The interpretation of these experiments using the ASTRA code [19] have taken into consideration all available measurements including bolometry, spectroscopic data, neutron data, magnetic sensors and Thomson scattering data [33]. The energy confinement time, plotted in the top panel of Fig. 6, exhibits the expected linear dependence on B_t , when $B_t \le 1$ T for both L- and H-mode plasmas. However, at around 1T, the increase in τ_E saturates, for both L- and H- mode plasmas.

Based on a plasma current scan, τ_E seems to have a near linear dependence on the plasma current, I_P , in agreement with the conventional tokamak scalings [29]. It is expected that the level of B_t where the τ_E saturates could increase with the increase of the plasma current.

For Globus-M2 scaling, for $B_t \leq 0.8T$, τ_E has been shown to be proportional to $B_t^{1.05}$ [32], while ST40 results for $B_t \leq 0.9T$ indicate an even stronger dependence: $\tau_E \sim B_t^{1.66}$. Ion heat diffusivity $\chi^{\rm ion}$, plotted normalised by the neoclassical ion heat diffusivity in the bottom panel of Fig. 6, is shown to be close to the neoclassical value at $B_t \sim 0.8T$. As B_t increases, $\chi^{\rm ion}$ increases and reaches a value of $\sim 4 \chi^{\rm ion}_{\rm neocl}$ at $B_t \sim 1.7T$, for H-mode plasmas. For L-mode plasmas, $\chi^{\rm ion} > 4 \chi^{\rm ion}_{\rm neocl}$ throughout the B_t scan.

4. HIGH-PERFORMANCE SCENARIOS

High performance scenarios with plasma current, I_p , reaching > 800kA in H-mode have been developed during the recent ST40 Campaigns. This has been achieved by carefully optimising the timing of the ramp-up phase and the transition into H-mode. Initially, the 450-500kA plasma from the MC start-up is kept small and limited with early NBI heating added for efficient current ramp-up to $I_p = 800$ kA. Around 40-50ms into the pulse, the plasma is then rapidly forced into diverted configuration after which it promptly enters H-mode. This allows for up to 50ms current flattops at Ip > 800 kA.

The high current H-mode pulses feature a steep density and modest temperature pedestals producing a 30-40% increase in stored energy (Fig. 7.). With early application of 1.7MW of NBI heating with both 24keV and 55keV neutral beams, the plasma initially reaches a hot-ion type scenario [34] with Ti \approx 2Te. These conditions are sustained into the H-mode until the temperatures equilibrate as the density increases and approaches $1.e10^{19}\ m^{-3}$. Good confinement with stored energy sustained at > 55 kJ has been demonstrated.

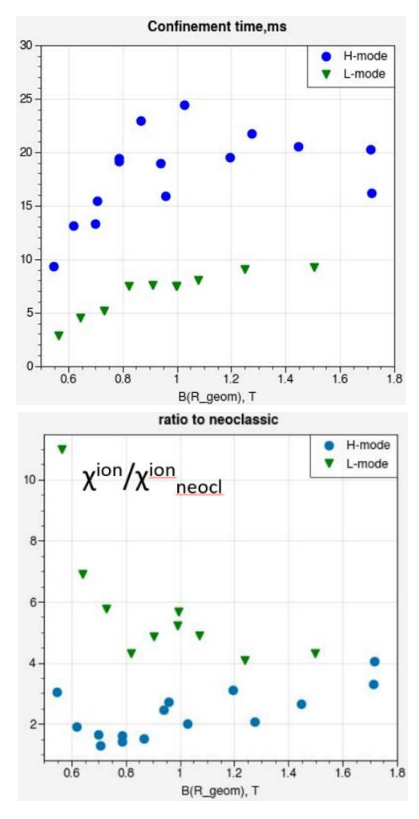


FIG. 6. Thermal confinement time (left panel) and ratio of ion current conductivity to its neoclassical value at the middle radius versus the toroidal magnetic field at the geometric axis B(R_{geom}) in the ST40 H- and L-mode series discharges. Data are averaged over the time between 100ms and 130ms.

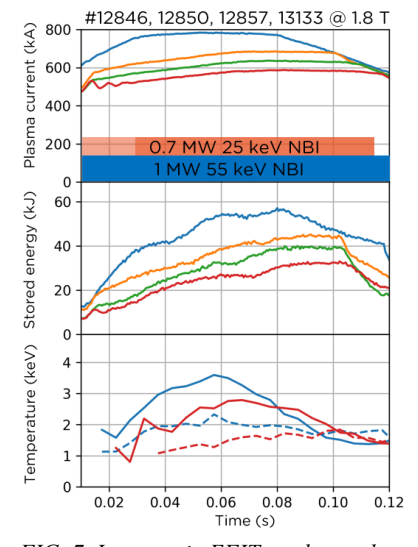


FIG. 7. Increase in EFIT total stored energy (middle panel) and T_i (bottom, solid) and T_e (bottom, dashed) with increasing I_p (top panel).

5. SCRAPE-OFF LAYER AND DIVERTOR

Divertor heat load is one of the key parameters driving the design of future ST pilot plants. Understanding it in existing devices, and predicting it in future devices, is of significant interest. To analyse the scrape-off-layer (SOL) power fall-off width (λ_q) in ST40, an infrared (IR) thermography analysis toolchain [35,36] has been implemented, utilising the IR camera facing the outer top divertor target. It combines (i) the measurement of surface heat flux on a section of the low-field-side region of the ST40 upper divertor (left top panel of Fig. 8), (ii) the 3D surface geometry of the divertor, and (iii) the magnetic geometry from the equilibrium reconstruction code EFIT and calculates the heat flux parallel to magnetic field lines in the SOL (left bottom panel of Fig. 8). Fitting these heat flux profiles with single and double exponential profiles has allowed extracting measurements of the power falloff width and revealed a bifurcation into a 'wide' branch that follows existing H-mode scalings and a 'narrow' branch that falls up to 10 times below the predictions of established scalings [37]. This bifurcation is apparent in the right panel of Fig. 8, where λ_q values are plotted as a function of the poloidal field at the outboard midplane, B_{θ} . The transition to the narrow branch has been correlated with steepened edge gradient, low edge collisionality, and transition into H mode [38]. The dataset for λ_q analysis, plotted in the right panel of Fig. 8, has been vastly expanded during the 2025 campaign, covering parameter space in B_t ranging from 0.9T to 1.8T, and B_{θ} , from 0.2T to 0.35T. Both wide and narrow branches are consistently observed at all plasma current and magnetic field values, and parallel heat fluxes up to 150MW/m² have been measured.

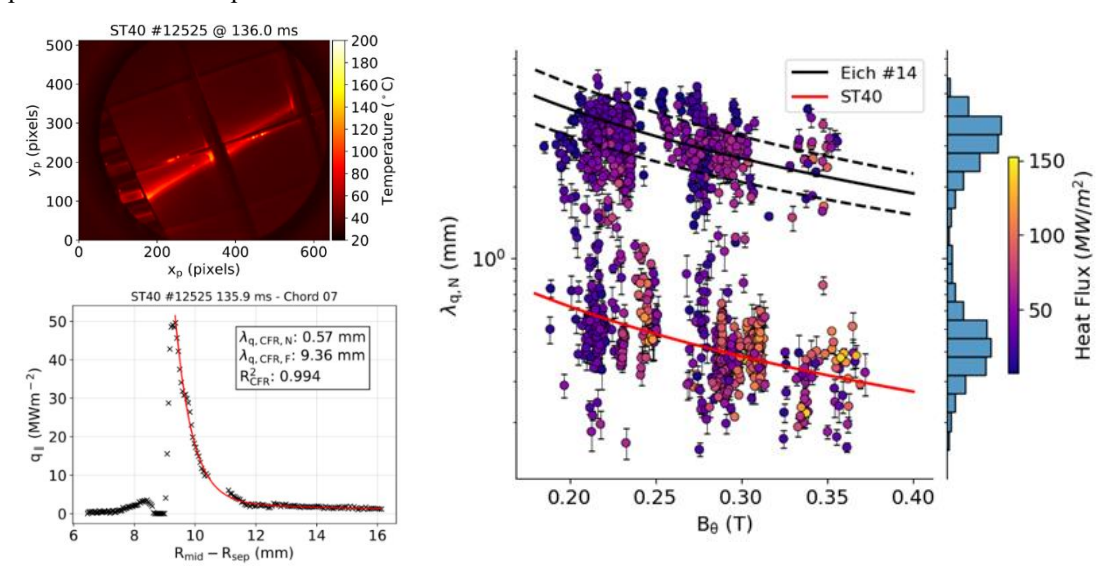


FIG. 8. Surface temperature measurements of the divertor by the infrared camera (top left) and parallel heat flux along a radial chord on the low-field-side upper divertor, mapped upstream to the outer midplane (bottom left). The data is fit with a double exponential profile, characterised by the near and far-SOL widths, $\lambda_{q,CFR,N}$ and $\lambda_{q,CFR,F}$. Dataset of λ_q plotted as a function of the poloidal field at the outboard midplane, B_{θ} , (right panel) exhibits the bifurcation into a 'wide' branch that follows existing H-mode scalings, and a 'narrow' branch.

6. LITHIUM EXPERIMENTS

Lithium granules with a diameter between 30-60 microns were injected into a variety of plasma scenarios. We consistently found that lithium had less of an effect at higher plasma performance. In the highest performance pulses where the dropper was used, $I_p \sim 750 \text{kA}$, $B_t \sim 2.1 \text{T}$, $n_{e0} \sim 1.\text{e}20/\text{m}^3$, $T_{e0} \sim 2 \text{keV}$, and $\sim 1 \text{MW}$ NBI at 55keV, lithium had no measurable effect on any core parameter, as can be seen in Fig. 9. By contrast, in lower performance scenarios, $I_p \sim 390 \text{kA}$, $B_t \sim 1.5 \text{T}$, $n_{e0} \sim 7e19/\text{m3}$, $T_{e0} \sim 1.5 \text{keV}$, $\sim 1 \text{MW}$ NBI at 55keV, lithium advanced the entry into H-mode, with no measurable change in Z_{eff} . More experiments are required to determine whether this effect is due to a change in edge density or a change in the H-mode power threshold.

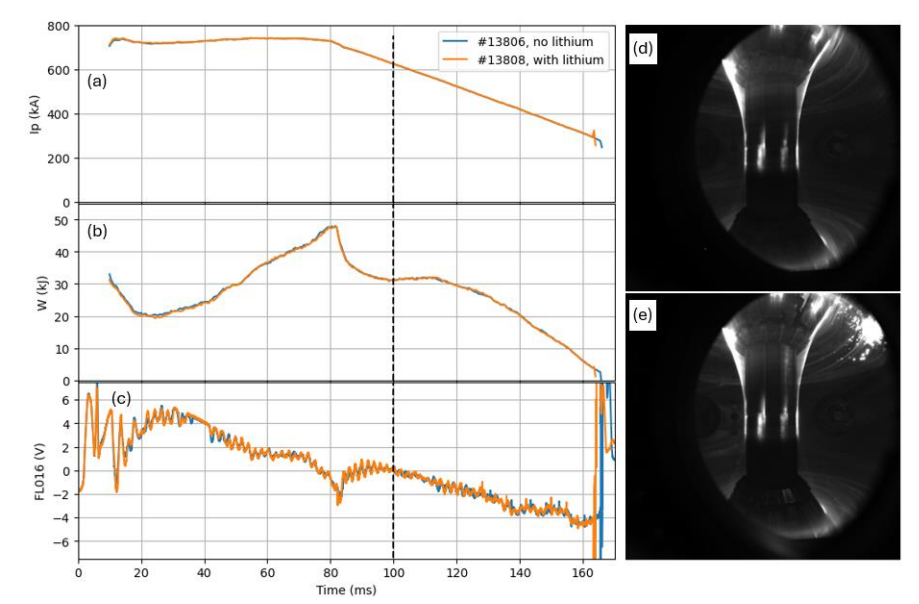


FIG. 9. Comparison of two high performance shots, no lithium #13806 (blue) vs with lithium #13808 (orange); (a) plasma current from GSFit; (b) stored energy from GSFit; (c) voltage from flux loop L016 located on the center post; (d)/(e) visible camera image from shot #13806/#13808.

7. UPCOMING UPGRADES

The main objectives of the next ST40 Programme, scheduled for 2027-2028, are to study (1) radiofrequency (RF) start-up, ramp-up and heating and current drive in a device with all metal PFCs, and (2) lower recycling regimes using the effect of lithium-coated PFCs. The balance between recycling, fuelling, and heating and current drive is of particular interest, as are the effects of lithium-coated walls on the scrape-off-layer, pedestal, and core confinement. To enable these studies, ST40 will go through an extensive upgrade. The shutdown will start before the end of 2025 and continue through most of 2026. This upgrade, and the Programme that follows, are funded primarily by a cross-governmental public-private partnership between Tokamak Energy, the U.S. Department of Energy, and UK Department of Energy Security and Net Zero [2]. They also build on the successful and continued collaborations between Tokamak Energy, Princeton Plasma Physics Laboratory (PPPL), and Oak Ridge National Laboratory (ORNL) [39].

The major projects during the upgrade are: (i) to replace ST40 graphite limiters with molybdenum plasma-facing components (PFCs), (ii) to furnish ST40 with hardware required for studying the effect of lithium-coated PFCs and, in particular, low wall recycling; (ii) to install and commission a 1MW dual-frequency (104/137 GHz) gyrotron for radio-frequency start-up, heating, and current drive; (iv) to install and commission a deuterium pellet injector for core fuelling; (v) to replace the ST40 centre column to improve robustness of the toroidal field coil joints and the central solenoid, and (vi) to overhaul the ST40 suite of diagnostics to support the objectives of the Programme. In addition to these major projects, a multitude of other improvements will be implemented throughout ST40 subsystems from controls to new gas lines and from power supplies to replacing a broken coil. Some of the major upgrade projects are discussed in more detail, below.

7.5. Radio-Frequency start-up, heating and current drive

A 1MW, dual-frequency, (104/137 GHz), 2s, gyrotron [40] is currently being installed. It will be operated from the next experimental Campaign onwards to provide electron-cyclotron resonance heating (ECRH). In addition to heating, the gyrotron will provide non-inductive current drive during plasma start-up, and plasma current rampup and flat-top phases. Both heating and current drive (H&CD) have been studied using ray-tracing code GENRAY [41] coupled to the transport codes ASTRA [19] and TRANSP [42].

Plasma heating using conventional second-harmonic extraordinary X2 mode wave has been investigated. Propagation and absorption of EC waves were explored either by a single ray or beam approximation description. The choice of the injection angles was dictated by the most efficient power absorption. To prepare for the upcoming gyrotron experimental campaign, time-dependent predictive scenario modelling using TRANSP was

performed to evaluate the impact of 1 MW EC H&CD at both 104 and 137GHz [43]. Two different ST40 pulses were used as the reference for TRANSP: pulse #11294 with no auxiliary heating and pulse #11336 with some NBI heating. Both were at nominal magnetic field of $B_t = 1.8T$ at R = 0.4m, which is readily achievable on ST40 as a standard operating point. For both scenarios, the impact of EC was relatively modest, resulting in a ~30% increase in central electron temperature and similar decrease in loop voltage, although there were signs of possible internal transport barrier formation whose influence was not included in the modelling. This modest result is likely due to the EC absorption not being central and instead being located mid-radius ($\rho \sim 0.4$) where electron transport effects are higher.

To have more central EC absorption, simulations with higher B_t were carried out with ASTRA/SPIDER. To imitate experimentally observed ST40 behaviour, the transport models chosen for the simulations were: prescribed H-factor model for electron temperature, and ion neoclassical transport for ion temperature. Electron density evolution, plotted in the bottom panel of Fig. 10, was prescribed and identical for all the four (4) cases: two values of toroidal magnetic field, $B_t = 2.1$ T and $B_t = 2.4$ T at R = 0.4m, two frequencies, 104GHz and 137GHz.

For the $B_t = 2.4T$, the peak core electron temperature, T_{e0} , at around 40ms, was 6keV, using the 104GHz. This was due to deposition location around $\rho \sim 0.1$ - 0.2 for 104GHz, while for 137 GHz it was moving from $\rho \sim 0.15$ to 0.45. For $B_t = 2.1T$, T_{e0} , reached 7keV for 104GHz. This was because at $B_t = 2.1T$ the X2 harmonic layer of the 104GHz wave is closer to the magnetic axis and the absorption stayed at $\rho = 0.1$. As the next step, the temperature might be increased more by placing an axis of a smaller-size plasma exactly at the resonance position and keeping it there during the whole duration of the pulse.

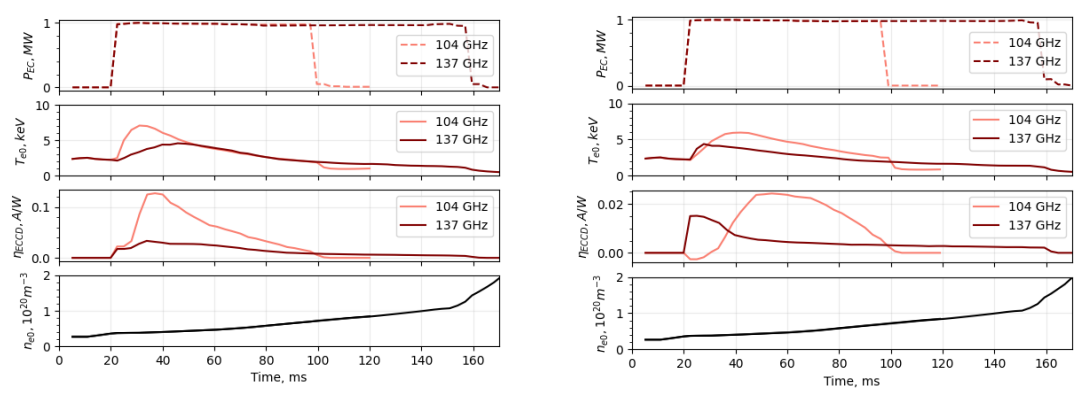


FIG. 10. Time evolution of power deposition (P_{EC}), central electron temperature (Γ_{e0}), current drive efficiency η_{ECCD} , and central density n_e for the case with Bt = 2.1T (left column) and Bt = 2.4T (right column).

Additionally, although EC current was generated, the ECCD efficiency only reached $\eta_{ECCD} \sim 0.02$ A/W since injection angles were not optimised to maximise η_{ECCD} : a typical value of the parallel refractive index was $|\mathbf{n}_{\parallel}| = 0.13$ -0.16, while optimal ones lie in the region $0.7 < |\mathbf{n}_{\parallel}| < 0.8$. The aim of this study, however, was to investigate possible T_e range for future scenarios. Along with the conventional ECRH modelling, predictions for the EC startup and ramp-up were made previously implementing O-X-B start-up scheme [44] and X1 schemes [45].

7.6. Lithium delivery and compatibility

The purpose of the lithium delivery system is to provide ST40 with the capability to safely perform controlled evaporations of lithium, in-vessel, to create clean lithium coatings on PFCs. To get even coating on all PFCs, two lithium evaporators will be designed and installed into ST40, in collaboration with PPPL. The evaporators will be installed on transfer arms that will bring them through the midplane ports, 180 degrees apart, to the middle of the vacuum chamber. They are designed for minimum shadowing to allow for maximum coverage.

To produce as clean lithium surfaces as possible, all graphite will be removed from inside ST40. This includes centre-column limiters, protective cuffs and bumpers, as well as neutral beam dumps. Removing graphite from ST40 is important for two reasons: (1) to minimise the amount of water in the vacuum chamber and (2) to avoid intercalation of lithium into graphite PFCs. Graphite readily absorbs water and gradually releases it over time. This, especially combined with the low (~100°C) baking temperatures of ST40, would make it difficult to achieve the low levels of water and oxygen impurities in the ST40 vacuum chamber that are desired to avoid oxidation of

the lithium coatings. Similarly, intercalation of lithium into graphite PFCs would prevent formation of clean lithium surfaces and, consequently, limit the ability of ST40 to achieve low recycling regimes.

A four-barrel deuterium pellet injector, designed and built by ORNL, will be installed on ST40 before the next experimental Campaign. While the pellet injector is important for other studies too, it is critical to lithium experiments as it can compensate for the low recycling caused by lithium coatings.

7.7. Diagnostics

To achieve the scientific goals of the next experimental Programme, the ST40 diagnostics suite will undergo significant upgrades. The functional upgrades are aimed at increasing the resolution of the plasma edge, where most of the effects from lithiumisation are expected to occur, to provide measurements that will be compatible with a full-metal wall, to support pellet fuelling studies, and, to generally increase resilience and maintainability of all diagnostic systems. The Thomson Scattering diagnostic will be equipped with new filters to access lower electron temperatures in the edge and SOL. It will also be modified to increase its resilience to mechanical and EM-induced vibrations. The TriWasp CXRS spectrometer [15] will be upgraded to higher spatial resolution and moved to S1 to view the HNBI beam from upstream to enable ion temperature and toroidal rotation measurements from the plasma centre to the LFS boundary. Multiple Lyman-alpha pinhole camera arrays viewing the central column and divertor PFCs will support edge neutral density studies. These measurements will be further supported by fast cameras measuring visible light and deuterium Balmer-alpha, and by a high-resolution passive spectrometer viewing the high-field-side PFCs from the low-field-side. This spectrometer will also be used to perform PFC erosion measurements and to correlate them with central impurity concentration measurements performed by the CXRS and XRCS systems. The spatial resolution of the top and bottom divertor Langmuir probe arrays will be increased, and their coverage will be extended to the inner divertor. A new IR camera and a new foil bolometer array will be installed to view the bottom divertor, providing an up-down symmetric diagnostic coverage of the ST40 divertors and plasma cross-section.

On top of the functional upgrades, additional boundary conditions imposed on the diagnostic systems are the introduction of radiofrequency H&CD, moving to molybdenum PFCs, and the addition of lithium wall conditioning capabilities. Many systems will be protected for stray ECRH radiation and Li deposition, and window transmission monitoring and cleaning capabilities from lithium deposits are being developed. Finally, absolute calibration of all neutron diagnostics is planned to take place just before the restart once all the systems have been re-installed on ST40.

ACKNOWLEDGEMENTS

We gratefully acknowledge the hard work and dedication of the ST40 team, and the support of the Tokamak Energy Board and shareholders. This work was supported in part by the U.S. Department of Energy under contract number DE-AC02-09CH11466 (PPPL), DE-AC05-00OR22725 (ORNL) and CRADAs NFE-19-07769 and NFE-24-10427. The United States Government retains a non-exclusive, paid-up, irrevocable, world-wide license to publish or reproduce the published form of this manuscript, or allow others to do so, for United States Government purposes. The 24 keV neutral beam system was provided on loan from Consorzio RFX.

REFERENCES

- [1] MCNAMARA, S.A.M., et al., Overview of recent results from the ST40 compact high-field spherical tokamak, Nucl. Fusion 64 (2024) 112020
- [2] U.S. DEPARTMENT OF ENERGY OFFICE OF SCIENCE, "DOE Partners with UK's DESNZ and Tokamak Energy Ltd. to Accelerate Fusion Energy Development through a \$52M Upgrade to the Privately Owned ST40 Facility", https://www.energy.gov/science/articles/doe-partners-uks-desnz-and-tokamak-energy-ltd-accelerate-fusion-energy-development
- [3] SYKES, A., et al., First results from the START experiment, Nucl. Fusion 32 (1992) 694
- [4] SYKES, A., et al., First results from MAST, Nucl. Fusion 41 (2001) 1423

- [5] BUXTON, P., PROKOPYSZYN, A.P., SERTOLI, M., GSFit: Grad-Shafranov Fit A new equilibrium reconstruction code for tokamak plasmas, submitted to Open Source Software for Fusion Energy Conference, Munich, Germany (2026)
- [6] TOKAMAK ENERGY LTD., GSFit: Grad-Shafranov Fit, GitHub repository (2025) https://github.com/tokamak-energy/gsfit
- [7] PROKOPYSZYN, A.P., *et al.*, RT-GSFit Real-time Grad-Shafranov Fit, submitted to Open Source Software for Fusion Energy Conference, Munich, Germany (2026)
- [8] LAO, L.L., *et al.*, Reconstruction of current profile parameters and plasma shapes in tokamaks, Nucl. Fusion **25** (1985) 1611
- [9] THE MATHWORKS INC., MATLAB version: 23.2.0 (R2023b), Natick, Massachusetts, United States, (2025) https://www.mathworks.com
- [10] SRIDHAR, S., et al., Optimizing Diagnostic Analysis Chain and Data Storage System in the ST40 fusion device, P31, Research Software Engineering Conference, Newcastle, UK (2024)
- [11] JETTE, M.A., WICKBERG, T., "Architecture of the Slurm Workload Manager" in Klusáček, D., Corbalán, J., Rodrigo, G.P. (eds) Job Scheduling Strategies for Parallel Processing. JSSPP 2023. Lecture Notes in Computer Science vol 14283. Springer, Cham, Switzerland.
- [12] COLGAN, C., et al., Soft x-ray tomography on the high field spherical tokamak ST40, Rev. Sci. Instrum. 95 (2024) 103501
- [13] HARRYMAN, D.M., et al., Design and commissioning of resistive foil bolometer diagnostics on the ST40 tokamak, Rev. Sci. Instrum. 95 (2024) 083534
- [14] SERTOLI, M., et al., From minimum-viable-products to full models: a step-wise development of diagnostic forward models in support of design, analysis and modelling on the ST40 tokamak, Plasma Phys. Control. Fusion 66 (2024) 095011
- [15] WILLETT, H.V., et al., TriWaSp: a multi-faceted visible spectroscopy diagnostic on the ST40 tokamak, JINST 18 (2023) C03023
- [16] WOOD, J., et al., Characterisation of ion temperature and toroidal rotation on the ST40 tokamak, JINST 18 (2023) C03019
- [17] GEMMELL, M., et al., "Bayesian Optimisation as a tool for solving the inverse problem with plasma diagnostics", 4 P 290, 51th European Physical Society Conference on Plasma Physics, Vilnius, Lithuania (2025)
- [18] JANKY, F., et al., SOPHIA: A tokamak simulator, Fusion Eng. Des. 222 (2026) 115447
- [19] PEREVERZEV, G.V., YUSHMANOV, Y.P., "ASTRA Automated System for TRansport Analysis in a tokamak", Tech. Rep. 5/42, IPP, Garching, Germany (1991)
- [20] IVANOV, A.A., et al., "New Adaptive Grid Plasma Evolution Code SPIDER", P5.063, 32nd European Physical Society Conference on Plasma Physics (2005)
- [21] DNESTROVSKIY, A.Y., et al., "Application of modified ASTRA-SPIDER code to simulation of free boundary equilibrium evolution", P4.1080, 45th European Physical Society Conference on Plasma Physics (2018)
- [22] ZOHM, H., et al., Investigation of the bifurcation character of the H-mode in ASDEX Upgrade, Plasma Phys. Control. Fusion 37 (1995) 437
- [23] COLCHIN, R.J., et al., Physics of slow L-H transitions in the DIII-D tokamak, Nucl. Fusion 42 (2002) 1134
- [24] SLADKOMEDOVA, A., et al., "Dynamics of plasma fluctuations and confinement properties during I-phase in ST40 plasmas", P2.4, 29th EU-US Transport Task Force Workshop, Budapest, Hungary (2025)

IAEA-CN-316/3337

- [25] BURRELL, K.H., et al., Creation and sustainment of wide pedestal quiescent H-mode with zero net neutral beam torque, Nucl. Fusion 60 (2020) 086005
- [26] GREENWALD, M., et al., Characterization of enhanced Dα high-confinement modes in Alcator C-Mod, Phys. Plasmas 6 (1999) 1943–1949
- [27] FAITSCH, M., et al., The quasi-continuous exhaust regime in ASDEX Upgrade and JET, Nucl. Mater. Energy 42 (2025) 101904
- [28] WADE, M., LEUER, J.A. Cost Drivers for a Tokamak-Based Compact Pilot Plant, Fusion Sci. Technol. 77 (2021) 119
- [29] VERDOOLAEGE, G., et al., The updated ITPA global H-mode confinement database: description and analysis, Nucl. Fusion 61 (2021) 076006
- [30] KAYE, S.M., et al., Confinement and local transport in the National Spherical Torus Experiment (NSTX), Nucl. Fusion 47 (2007) 499
- [31] VALOVIČ, M., et al., Scaling of H-mode energy confinement with Ip and BT in the MAST spherical tokamak, Nucl. Fusion 49 (2009) 075016
- [32] KURSKIEV, G.S., et al., Energy confinement in the spherical tokamak Globus-M2 with a toroidal magnetic field reaching 0.8 T, Nucl. Fusion 62 (2022) 016011
- [33] DNESTROVSKII, A., et al., "Dependence of confinement on magnetic field in the ST40 spherical tokamak", P1.14, 29th EU-US Transport Task Force Workshop, Budapest, Hungary (2025)
- [34] MCNAMARA, S.A.M., *et al.*, Achievement of ion temperatures in excess of 100 million degrees Kelvin in the compact high-field spherical tokamak ST40, Nucl. Fusion **63** (2023) 054002
- [35] MARSDEN, C., et al., Inferring the scrape-off layer heat flux width in a divertor with a low degree of axisymmetry, Nucl. Mater. Energy 41 (2024) 101773
- [36] MOSCHENI, M., et al., Measurement of divertor surface heat flux by infra-red thermographic inversion in ST40, Rev. Sci. Instrum. 96 (2025) 013503
- [37] ZHANG, X., et al., Experimental observations of bifurcated power decay lengths in the near Scrape-Off Layer of ST40 High Field Spherical Tokamak, Nucl. Mater. Energy 41 (2024) 101772
- [38] ZHANG, X., et al., Core-edge integrated predictive studies of ST40 and NSTX plasmas with the scrape-off layer box model, Phys. Plasmas 32 (2025) 032513
- [39] MCNAMARA, S., et al., The ST40 Collaboration: A Groundbreaking, First-of-Its-Kind, Public-Private Partnership in Fusion, Fusion Sci. Technol. (2025) 1-14
- [40] YAGASAKI, K., et al., A high-power oscillation test of a dual-frequency 1 MW gyrotron, Fusion Eng. Des., 218 (2025) 115143
- [41] HARVEY, R.W., MCCOY, M.G., Proceedings of the IAEA Technical Committee on Advances in Simulation and Modeling of Thermonuclear plasmas, 489, Vienna, IAEA. (1993)
- [42] HAWRYLUK, R., "An Empirical Approach to Tokamak Transport", in Physics of Plasmas Close to Thermonuclear Conditions, ed. By B. Coppi et al. (CEC, Brussels, 1980), Vol. 1, pp. 19-46
- [43] LOPEZ, N, et al., Time-dependent modelling of 104/137 GHz X2-mode ECRH on ST40 to aid future scenario development, submitted to EPJ Web of Conf. (2025)
- [44] DU TOIT, E.J., SHEVCHENKO, V.F., Development of an electron cyclotron resonance heating and electron Bernstein wave current drive system on ST40, Plasma Phys. Control. Fusion 64 (2022) 115015
- [45] ONO, M., BERTELLI, N., SHEVCHENKO, V., Multi-harmonic electron cyclotron heating and current drive scenarios for non-inductive start-up and ramp-up in high field ST-40 spherical tokamak, Nucl. Fusion, 62 (2022) 106035